



# *Anisotropy analysis of 2D and 3D textures using anisotropic fractional Brownian field*

Ferdaous OUERTANI

Dep. Of Maths and Informatics, Paris Descartes  
Paris, France  
ferdaous.ouertani@gmail.com

## *Abstract*

**This paper aims first at implementing two algorithms to extract Region Of Interest (ROI) from 2D (mammography) and 3D images (tomosynthesis) so that to gather ROI databases and second, at analyzing anisotropy of these images textures using an anisotropic fractional Brownian field to check whether the model being studied helps apprehend the breast anisotropy. This analysis includes the estimation and the comparison of indices (already presented in [17]). We detail two algorithms: the automatic and the manual extraction of ROI implemented to gather 2D and 3D Region Of Interest (ROI) databases. Tests performed are described and results are reported.**

*Keywords-medical imaging, fractional Brownian fields, tomosynthesis, mammography, anisotropy, texture.*

## I. INTRODUCTION

Medical imaging techniques have revolutionized health care delivery around the world. Melding medical imaging advances with the power of digital and information technology that is offering highly personalized and targeted means of powerful diagnosis generation is fostering greater quality and efficiency in health care.

Depending on the imaging modality, the resulting images are whether 2D or 3D. In the present work, we will be restricted to the analysis of mammographic images as 2D ones and tomosynthesis images as 3D ones. To take advantage from information provided by these images, these ones are analyzed based on different aspects. Texture consists one of these aspects.

Considered as a periodic aspect of images, texture has been modeled using various mathematical approaches.

In the current work based on the model definition of [17], texture analysis is performed from a probabilistic point of view considering the image as a realization of a random field whose properties reflect those of the texture.

Model definitions have varied depending on texture properties among which texture anisotropy is one of the most important. It can be apprehended using some directional processes that are either defined as a restriction of the image on an oriented line or as a projection of the image along a given direction [17]. Anisotropy can then be analyzed by looking at regularity variations of these processes when the extraction direction changes.

In this work we propose two algorithms to extract ROI from either mammography or tomosynthesis. We describe a tool for image segmentation and region of interest (ROI) extraction (under some specific conditions) to end-up with gathering the 2D and 3D extracted ROI into two databases. We also analyze anisotropy of the images textures using an anisotropic fractional Brownian field whose definition is presented in the next section of this paper. We perform statistical tests on the ROI databases to check whether the model being studied is adequate and if it helps apprehend the anisotropy of the breast. In this context, it makes sense to note that images segmentation, which is a key step for the ROI extraction, is a difficult and very important part of the current work. A wrong segmentation can invalidate all the processing steps that come after and thus lead to a wrong analysis.

This paper is organized as follows: In the first part, we summarize materials and methods: We make an overall presentation of the anisotropic fractional Brownian field model used as well as a brief description of mammography and tomosynthesis. We also describe the algorithms used and the different steps followed so that to exploit and analyze the images database. In the second part, we expose the different statistical tests performed and discuss results.

## II. MATERIALS AND METHODS

### A. *Anisotropic Fractional Brownian Field (AFBF)*

#### *a) Introduction*

Textures are normally ranging from micro (statistical textures) to macro (structural textures), and depending on the texture type, several models (namely structural models, probabilistic models,...) can be used to represent it [4]. In the current work, tissues we analyze via mammograms and tomosynthesis will restrict us to statistical textures and the approach is to consider it as a realization of a random field.

b) Model presentation

It has been put forward that anisotropy can be captured from processes extracted from the image [3] [17], either line-process defined by restricting the image on oriented lines of the image domain, or projection-process obtained by projecting the image parallel to a given direction. From these processes, anisotropy can be analyzed by looking at their regularity variations when the extraction direction changes. In the sequel, we present the AFBF model used in this work referring to the model presented by Frederic Richard and Hermine Bierme in [16] and [17].

Description:

The anisotropic fractional Brownian field is mathematically defined as the unique centered Gaussian field, null at origin, with stationary increments and self similar of order  $H \in (0, 1)$ . Parameter  $H$ , called the Hurst index, is a fundamental parameter which is an indicator of texture roughness. [3], [16], [10] and [17].

Its variogram, which is of the form (1.1) is characterized by a positive function  $f$  called spectral density. This function is of the form (1.2).

$$\forall x \in \mathbb{R}^d, v(x) = \int_{\mathbb{R}^d} |e^{ix \cdot \zeta} - 1|^2 f(\zeta) d\zeta, \quad (1.1)$$

$$\forall \zeta \in \mathbb{R}^2, f(\zeta) = |\zeta|^{-2h(\arg(\zeta)) - 2}, \quad (1.2)$$

where  $\arg(\zeta)$  is the direction of the frequency  $\zeta$  and  $h$  is a measurable periodic function ranging in  $[H; M] \subset (0; 1)$  with:  $H = \text{essinf } h(\theta)$  and  $M = \text{esssup } h(\theta)$ .

Since its spectral density  $f$  depends on the spectral direction  $\arg(\zeta)$ , this model is anisotropic.

Its anisotropy is characterized by parameters whose estimation characterizes the anisotropy of the field.

In [3], Bonami and Estrade proposed to use windowed Radon transforms of a field to get information about its anisotropy. These transforms are defined for any direction  $\theta$  of  $\mathbb{R}^3$  by projecting a field  $X$  along lines of  $\mathbb{R}^3$  directed by  $\theta$ . With:  $\theta \perp \perp \theta$ .

Given a window function  $\rho$  of the Schwartz class such that  $\int \rho(\gamma) \delta\gamma = 1$ , the projection of  $X$  along lines oriented in the direction  $\theta$  through the window  $\rho$  is defined as follows:

$$\mathcal{P}_{X, \theta} = p(X, \theta)(y) = \int X(y\theta + z\theta^\perp) \rho(z) dz \quad (1.3)$$

As mentioned, the Hurst index  $h(q)$  of an anisotropic fractional Brownian field in a given direction  $\theta$  can be deduced from the Hurst index of the projected field

perpendicular to this direction. Consequently the problem of estimating the directional Hurst index of an AFBF reduces to the problem of estimating the Hurst indices of projected fields [16]. Let  $f$  be a projection angle and let  $\theta = (\theta_x, \theta_y, \theta_z)$  then, if we refer to fig.1

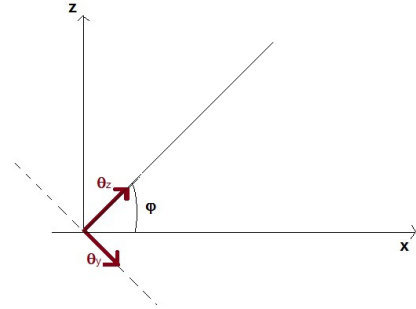


Figure1. The  $\theta$  projection

$$\begin{aligned} \theta_x &= (1, 0, 0) \\ \theta_y^\phi &= (0, -\sin(\phi), \cos(\phi)) \\ \theta_z^\phi &= (0, \cos(\phi), \sin(\phi)) \end{aligned}$$

In [17], some estimators of the parameters  $h(\theta_x)$ ,  $h(\theta_y)$  and  $h(\theta_z)$  are proposed based on projections and quadratic variations.

These estimators differ in two categories defined as follows:

- Estimators obtained by projecting the field  $X$  along lines oriented in the direction  $\theta \perp$  through the window  $\rho$  (previously described) which are:  $\hat{h}^1$ : estimator of  $h(\theta_x)$ ,  $\hat{h}^2$ : estimator of  $h(\theta_y)$
- Estimators obtained by restriction of the field  $X$  on a line, which are:  $\hat{h}^0_1$  and  $\hat{h}^0_2$ , estimators of  $\min h(\theta)$  (The reader is referred to [14] and [17] for detailed explanation).

It was proved in [3] that the Hölder regularity of the projected field  $\mathcal{P}_{X, \theta}$  is equal to  $h(\theta) + 1/2(d-1)$  for all directions  $\theta$  of  $\mathbb{R}^d$ . In the case of  $d = 3$ ,  $\mathcal{P}_{X, \theta}$  regularity is equal to  $h(\theta) + 1$ .

$$\mathcal{P}_x(t) = \int X(t\theta_x + r\theta_y + s\theta_z) \rho(r) \rho(s) dr ds \quad (1.4)$$

whose regularity is  $h(\theta_x) + 1$ .

$$\mathcal{P}_y(t) = \int X(r\theta_x + t\theta_y + s\theta_z) \rho(r) \rho(s) dr ds \quad (1.5)$$

whose regularity is  $h(\theta_y) + 1$ .

B. Imaging Modalities

a) Mammography

Mammography is a type of imaging that, by the use of a dose of x-ray system, helps examine breasts and detect changes in tissues before they are noticeable or visible.

This technique provides two-dimensional information that allows the radiologist to make a diagnosis.

b) Tomosynthesis

A technique, which, from a set of projection images acquired as the X-ray tube moves along a prescribed path, enables the reconstruction of multiple section images. In fact, by combining projections, it is possible to reconstruct the three-dimensional projected volume and thus to obtain 3D information on the organ examined. [7] fig.2 illustrates one among Tomosynthesis acquisition techniques.

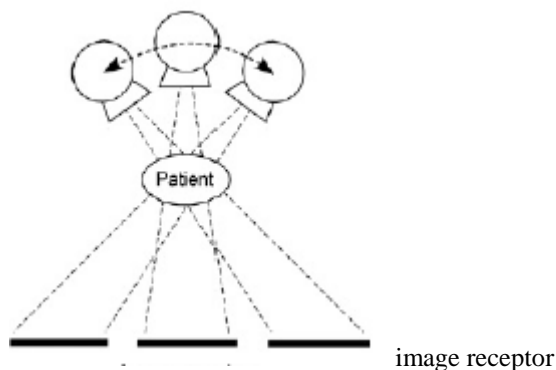


Figure2. Tomosynthesis acquisition technique

C. Database description

The current work is done in collaboration with the department of Radiology, University of Pennsylvania, that have provided the database of breast tomosynthesis and mammography on which we have performed our tests.

This database includes information about 40 patients: For each patient, nine projections for the breast tomosynthesis and three mammographies are provided.

For the tomosynthesis cases, each projection was done under 6.25 degrees to each other. The distance from the detector to the pivot point (i.e., the center of tube rotation) was 20 cm. The distance from the pivot point to the x-ray tube (i.e., focal spot) was 46 cm. (Thus the distance from the detector to the focal spot for the orthogonal projection was 66cm.)

This information is useful to implement the second algorithm described in the next section.

D. Methods

Two Region of Interest (ROI) extraction methods were developed:

a) An automatic method: where the extraction of the ROI is automatically computed according to specific conditions.

To automatically extract the region of interest, it comes to distinguish the three big parts that form a given image in the database previously described. These three parts are visible

to the unaided eye, namely, the collimator, the breast and the background.

- Background segmentation  
It makes sense here to note that the threshold value is computed based on Otsu's method.
- Collimator segmentation

A collimator is a device that allows only the rays going parallel to a particular direction to pass, and this is by filtering these rays. For this reason, depending on the source angle, some of the resulting images lose some or most of their information. After being exposed to the x-rays, in the resulting image, the collimator area appears to be less opaque than the whole image.

A possible solution to segment the collimator is to use the standard deviation.

In fact, for each line in the image, its standard deviation is calculated (as shown in fig.3 (a) and (2.1)) with  $line = image(i,:)$

$$s(i) = \text{std}(line), \quad (2.1)$$

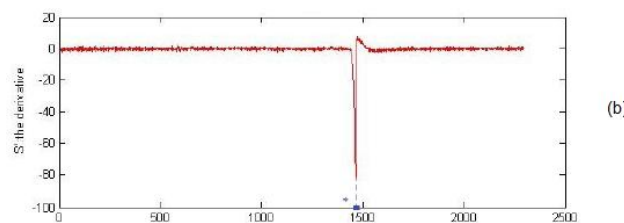
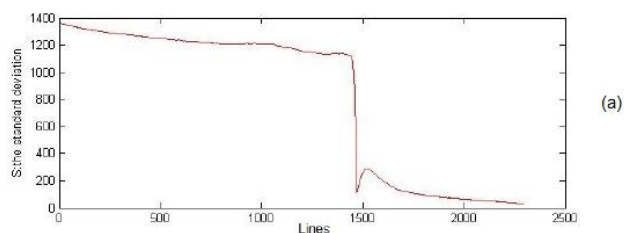


Figure3.Collimator segmentation

The derivative is applied, computing thus the rate at which the standard deviation changes with respect to the change in the image lines (2.2).

$$S^2 = \text{diff}(s), \quad (2.2)$$

This standard deviation derivative with respect to the image lines allows locating and thus segmenting the collimator (as illustrated in fig.2.2 (b)). Its location corresponds to the position of the pick,

Once the collimator location is known and having the binary labeled image, objects and boundaries are localizable. We can separate the three parts of the image by assigning a label to every pixel as shown in the fig.4

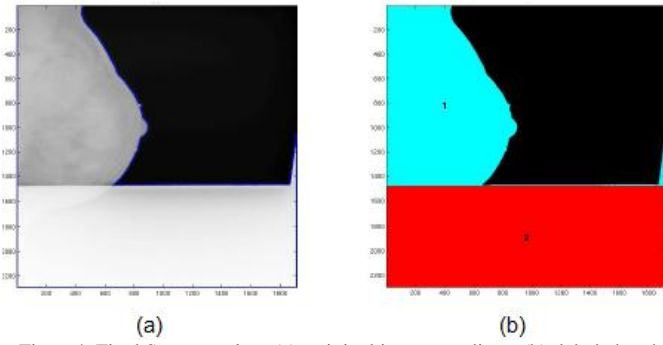


Figure4. Final Segmentation, (a): original image+outlines, (b): labeled and colored regions

- Axis and region of interest localization

At this level, our purpose is to locate the optimal position from which a region of interest will be extracted. To do this, we have to understand the breast structure and which area of the breast is more likely to be most interesting for our analysis.

Breast structure :

The breast is an organ composed mainly of fatty tissue which also has milk glands contained within it. A series of ducts connect the milk glands to the nipple [20].

The breast is rich in blood vessels and lymphatic channels. (fig.5)

Breast cancer develops from breast tissue, almost from the internal lining of milk ducts or the lobule that supply the ducts with milk.

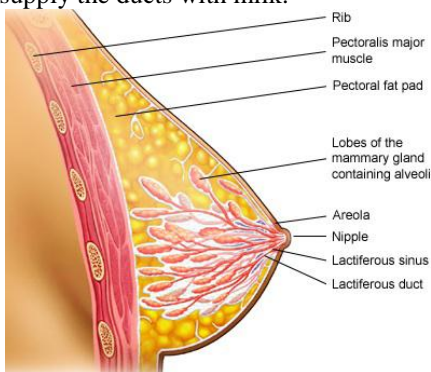


Figure5. Breast structure (Figure adapted from [20] )

Ductal carcinomas is the appellation of cancers originating from ducts whereas lobular carcinomas is the appellation of those originating from lobules.

Region of interest axis:

Based on the breast structure, the region of interest extracted should be as close as possible to the nipple. In practice, we browse the image and, in the region labeled as the breast part (label (1) in fig.4-(b)), we select the furthest point that constitutes the nipple as shown in fig.5.

Given its size, the ROI must fulfill conditions including the fact that it must not exceed the limits of

the breast. That is why, for one patient, it is not always necessary to find that all the projections are exploitable (fig.7).

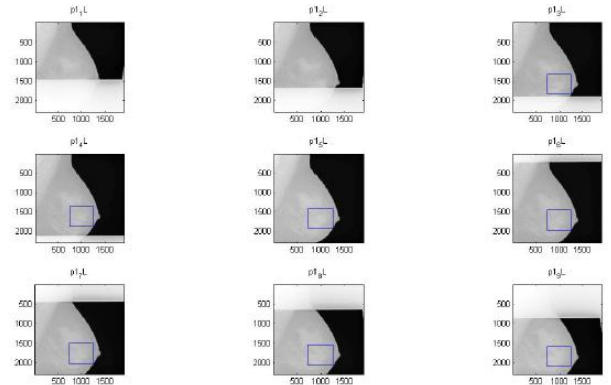


Figure7. The ROI extracted from each of the nine projections (if allowed) of each patient

b) A manual method: where the ROI is defined manually by the user.

In this part, we will refer to the tomosynthesis reconstruction strategy defined in [7] based on the fact that tomosynthesis means, commonly, generating a set of slice images from the summation of a set of shifted projection images acquired at different orientations of the tube.

Assuming that the x-ray tube and the detector each move in a linear path along the x-direction, the function for linear-motion tomosynthesis may be derived by considering the imaging geometry depicted in fig.8.

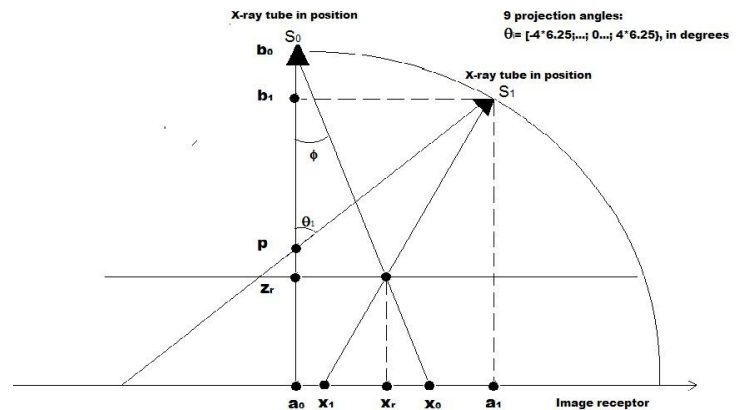


Figure8. Tomosynthesis reconstruction geometry

The idea here is to manually choose and extract a ROI from the fifth projection (which is the projection of reference) among the nine others and automatically compute the coordinates of this extracted ROI in the other projections. In this figure, for the first projection image, the x-ray tube is at location  $x = x_0$  and the detector is centred at location  $x = a_0$ . The fulcrum plane about which the tube and detector move in synchrony is at height  $p$ . The x-ray tube is at height  $z = b_0$  above the plane of the detector.

Let  $z_r$  be the half height of the breast,  $S_i(a_i, 0, b_i)$ : the x-ray tube source and  $R(x_r, y_r, z_r)$  the reference point. Given these coordinates  $(x_0, y_0, z)$ , our purpose is to find out  $T(x_i, y_i, z)$ .

In this geometry, it may be demonstrated that:

If  $\Delta_{SR}$  is a line through the points S and R, then:

$$\Delta_{SR} = \{ M(x, y, z); SM = \alpha SR \} \quad (2.3)$$

According to (2.3):

$$(x - a_i) = \alpha (x_r - a_i) \quad (2.4)$$

$$(y - 0) = \alpha y_r \quad (2.5)$$

$$(z - b_i) = \alpha (z_r - b_i) \quad (2.6)$$

$$T(x_i, y_i, z) = \Delta_{SR} \cap \{z = 0\} \text{ This leads to } \alpha = (b_i) / (b_i - z_r) \quad (2.7)$$

$$x_i = \alpha(x_r - a_i) + a_i \quad (2.8)$$

$$y_i = \alpha y_r \quad (2.9)$$

with  $a_i$  and  $b_i$  are the x-ray tube coordinates.

Referring to the fig.8, the location of the x-ray tube may be shown to be:

$$b_i = \cos(\theta_i) (b_0 - p) + p \quad (2.10)$$

$$\text{Having } \cos(\theta_i) = (b_i - p) / (b_0 - p) \text{ and } a_i = \sqrt{(b_0 - p)^2 - (b_i - p)^2} \quad (2.11)$$

### III. TESTS AND RESULTS

Our tests aim at computing and comparing on each projection the four indices mentioned in the first part, which are:  $H_{01}$ : on horizontal line;

$H_{02}$ : on vertical line;

$H_1$ : on horizontal projection;

$H_2$ : on vertical projection;

Our tests treat NaN values as missing data, and ignore them.

#### A. Tomosynthesis

Tests are realized on ROI extracted according to the first algorithm presented in the last part of the paper, which is based on the automatic extraction.

The parameter  $v$ , one of the important parameters present in our tests, presents the subsampling factor; In fact, when discretizing each projection, there is an estimation bias. To compensate this bias, each projection is subsampled with a subsampling factor of  $2v$ . The bigger this parameter is, the smaller the bias is and the bigger the variance is.

In the sequel, we expose results obtained from varying this parameter  $n$  twice.

- a) ROI size= 512,  $v = 3$ 
  - $H_{01}, H_{02}$  equality test

The global regularity is being measured at first. For this, we use the ANOVA test so that to check the correlation between  $H_{01}$  and  $H_{02}$ , and we fix a hypothesis test to the following:

Assuming that  $N$  is the global number of projections, the linear model is of the form:

$$H_{01,i} = \mu_1 + \epsilon_i \text{ with } i = 1, \dots, N$$

$$H_{02,i} = \mu_2 + \epsilon_i$$

The null-hypothesis being tested is  $H_0: \mu_1 = \mu_2$  against the alternative one  $H_1: \mu_1 \neq \mu_2$

The estimates of the minimal Hurst index we obtained using line-based estimators on the extracted regions of interest are with an average of  $\approx 0.11$  and a standard deviation of 0.12.

In fig.9, it's shown that the line-based estimates of the minimal Hurst in both directions are almost equal on each image and have equivalent empirical distributions.

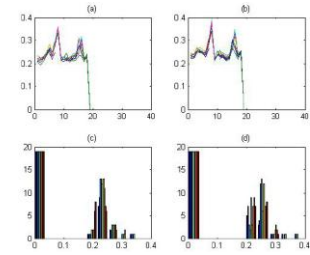


Figure9.  $H_{01}$  (a) and  $H_{02}$  (b) distributions; (c) and (d) are the respective histograms

This observation is reinforced by the ANOVA test, illustrated in fig.10, in which the p-value is equal to 0.5767.

Assuming that the significant risk level is about 0.05, this value (p-value) suggests that data are not inconsistent (at this level of risk) with the null hypothesis which is the means equality. Thereby, we conclude that:

$$H_{01} = H_{02} = H_0 \approx 0.11 \pm 0.12.$$

| ANOVA Table |         |     |         |      |        |
|-------------|---------|-----|---------|------|--------|
| Source      | SS      | df  | MS      | F    | Prob>F |
| Columns     | 0.00475 | 1   | 0.00475 | 0.31 | 0.5767 |
| Error       | 9.44341 | 620 | 0.01523 |      |        |
| Total       | 9.44816 | 621 |         |      |        |

Figure10. Anova Test

- $H_1$  equality test

The second test measures the regularity in the horizontal direction.

The estimate of the horizontal Hurst index we obtained using projection based estimator on the extracted regions of interest is with an average of  $H_1 \approx 0.15$  and a standard deviation of 0.19.

Let  $H_{j,i}$  be  $H_1$  estimated on the  $j$ th projection of the  $i$ th acquisition,  $j_0 = 5$  the projection reference and

$$\delta j_{1,i} = H_{j1,i} - H_{j0,i}$$

$$\delta j_{1,i} = \mu + \epsilon_i$$

By performing the t-test on our data, we aim at demonstrating one of these assumptions:

The null-hypothesis  $H_0: \mu = 0$  against the alternative one  $H_1: \mu \neq 0$ .

Results are reported in tables 1, 2 and 3.

TABLE1.  $H_{j1,i}$  MEANS,  $v = 3$

|      | Projections |      |      |      |      |      |      |      |      |
|------|-------------|------|------|------|------|------|------|------|------|
|      | 1           | 2    | 3    | 4    | 5    | 6    | 7    | 8    | 9    |
| Mean | 0.07        | 0.12 | 0.16 | 0.18 | 0.18 | 0.17 | 0.14 | 0.14 | 0.13 |
| Std  | 0.13        | 0.16 | 0.19 | 0.20 | 0.22 | 0.23 | 0.17 | 0.19 | 0.19 |

TABLE2.  $\delta j_{1,i}$  MEANS,  $v = 3$

|      | Projections |       |       |       |      |       |       |       |  |
|------|-------------|-------|-------|-------|------|-------|-------|-------|--|
|      | 1           | 2     | 3     | 4     | 6    | 7     | 8     | 9     |  |
| Mean | -0.04       | -0.03 | -0.01 | -0.01 | 0.00 | -0.03 | -0.03 | -0.03 |  |
| Std  | 0.12        | 0.10  | 0.11  | 0.12  | 0.12 | 0.09  | 0.10  | 0.10  |  |

TABLE3.  $H_1$  T-TEST,  $v = 3$

|         | Projections |      |      |      |      |      |      |      |  |
|---------|-------------|------|------|------|------|------|------|------|--|
|         | 1           | 2    | 3    | 4    | 6    | 7    | 8    | 9    |  |
| p-Value | 0.07        | 0.07 | 0.43 | 0.81 | 0.99 | 0.06 | 0.12 | 0.05 |  |
| Reject  | 0           | 0    | 0    | 0    | 0    | 0    | 0    | 1    |  |

Fig. 11 shows that in almost all the projections, for each one, the estimate of the horizontal Hurst index is equal to the one of the reference projection. At the 5% significance level, the t-test indicates a failure to reject the null hypothesis, which means that there is an isotropy in  $H_1$ . This result seems logical since we are dealing with the same angle in the horizontal axis.

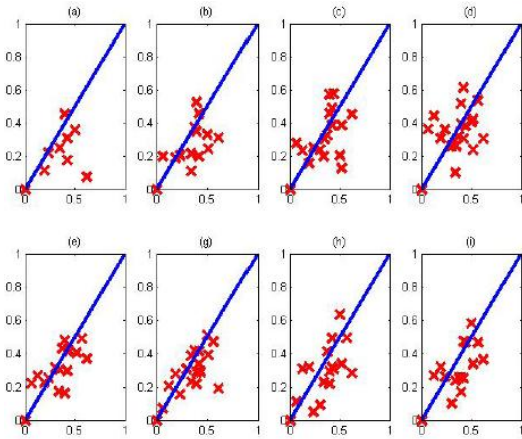


Figure11.  $H_1$  Equality test, (a), (b), (c), (d),(e),(f), (g), (h) represent the  $H_1$  estimate correlations between the reference projection and respectively the first, second, third, fourth, fifth, sixth, seventh and eighth one

- **$H_2$  equality test**

We focus now at measuring the regularity in the vertical direction. The estimate of the vertical Hurst index we obtained using projection-based estimator

on the extracted regions of interest is with an average of  $H_2 \approx 0.12$  and a standard deviation of 0.18.

As for the horizontal estimation, let  $H_{j2,i}$  be  $H_2$  estimated on the  $j$ th projection of the  $i$ th acquisition,  $j_0 = 5$  the projection reference and:

$$\delta j_{2,i} = H_{j2,i} - H_{j_0 2,i}$$

$$\delta j_{2,i} = \mu + \epsilon_i$$

As we proceeded in the  $H_1$  test, we perform a t-test on our data under the null-hypothesis  $H_0: \mu = 0$  against the alternative one  $H_1: \mu \neq 0$ .

Results showed that, at the 5% significance level, the t-test indicates a failure to reject the null hypothesis. In other words, anisotropy, at the level of 5%, could not be detected.

- **$H_1, H_2$  equality test**

In this part, our interest is to measure the regularity by testing the difference between indices in the horizontal and vertical direction.

For this, we apply a t-test on our data under the null-hypothesis

$H_0: \mu_j = 0$  against the alternative one  $H_1: \mu_j \neq 0$ .

with  $\mu_j$  is defined as follows:

Let  $H_{j1,i}$  and  $H_{j2,i}$  be respectively  $H_1$  and  $H_2$  estimated on the  $j$ th projection of the  $i$ th acquisition,

$$\delta_{j,i} = H_{j1,i} - H_{j2,i}$$

$$\delta_{j,i} = \mu_j + \epsilon_{ji}$$

Results indicate that, at the 5% significance level, the t-test failed to reject the null hypothesis and therefore, to detect anisotropy.

These results could be explained by the choice of some of our parameters( $v$  for example).

In fact, the smaller this parameter is, the more biased the estimator is.

In what follows, the  $v$  parameter value is increased so that to decrease the bias.

- b) **ROI size= 512,  $n = 4$**

The same procedure is repeated to study the regularity, by increasing our sub sampling parameter  $v$ . Results are described as follows: The estimates of the minimal Hurst index we obtained using line-based estimators on the extracted regions of interest are with an average of  $\approx 0.25$  and a standard deviation of 0.03.

The estimate of the horizontal Hurst index obtained using projection-based estimator on the extracted regions of interest is with an average of  $H_1 \approx 0.39$  and a standard deviation of 0.16.

When it comes to regularity in the vertical direction, the estimate of the vertical Hurst index obtained

using projection-based estimator on the extracted regions of interest is with an average of  $H_2 \approx 0.39$  and a standard deviation of 0.15.

The difference between  $H_1$  and  $H_0$  as well as the difference between  $H_2$  and  $H_0$  casts doubt on isotropy.

The same t-test previously performed is applied to our data with the new parameter and results showed that, at the 5% significance level, there is an isotropy in  $H_1$ .

As previously mentioned, this result seems logical since we are dealing with the same angle in the horizontal axis.

When it comes to the vertical direction, at the 5% significance level, anisotropy is detected on some projections according to table4.

TABLE4. H2 T-TEST,  $v = 4$

|         | Projections |      |      |      |      |      |      |      |  |
|---------|-------------|------|------|------|------|------|------|------|--|
|         | 1           | 2    | 3    | 4    | 6    | 7    | 8    | 9    |  |
| p-Value | 0.04        | 0.41 | 0.03 | 0.45 | 0.41 | 0.39 | 0.41 | 0.32 |  |
| Reject  | 1           | 0    | 1    | 0    | 0    | 0    | 0    | 0    |  |

### B. Mammography

In this section, our objective is to study the x-ray dose effect through the comparison between mammograms and tomosynthesis projection for each index (we will take the fifth projection as the reference one).

Mammograms used in this test are those whose view is MedioLateral Oblique: MLO.

In the sequel, tests will be performed as follows: for both mammograms and the fifth projection of each patient, the four indices will be computed, and then we will compare each index computed on the two types of image, in other words, to compare  $H_{0,i}$  computed on both mammograms and the fifth projection, we use the following test:

$H_{0,5,i}$  be  $H_{0i}$  estimated on the 5th projection of the  $i$ th acquisition, and  $H_{0,M,i}$  be  $H_0$  estimated on the mammogram of the  $i$ th acquisition, and

$$\delta_{0,i} = H_{0,5,i} - H_{0,M,i}$$

$$\delta_{0,i} = \mu + \epsilon_i$$

By performing the t-test on our data, we aim at demonstrating one of these two assumptions:

The null-hypothesis  $H_0: \mu = 0$  against the alternative one  $H_1: \mu \neq 0$ .

Results cast doubt on the null-hypothesis and allow us to conclude that, at 5% significance level, there is no equality between the fifth projection and the mammogram on  $H_{0,i}$  on the horizontal line.

This result is illustrated in fig.12 where the x axis represents the estimates of  $H_{0i}$  on the 5th projections and the y axis is the estimates of  $H_{0i}$  on the mammograms.

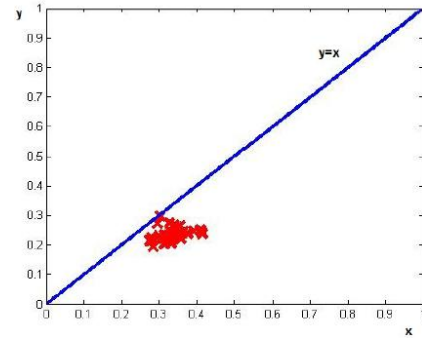


Figure12. H01 Equality test between the reference projection and mammography

The same t-test procedure is repeated to test equality between the fifth projection and the mammogram on  $H_{0,i}$  on the vertical line, on  $H_1$  on the horizontal projection and on  $H_2$  on the vertical projection.

Having a p-value under the 5% significance level, all the obtained results reject the null - hypothesis of equality between mammograms and the reference projections (at this level) on all the indices. Fig.13 illustrates this inequality.

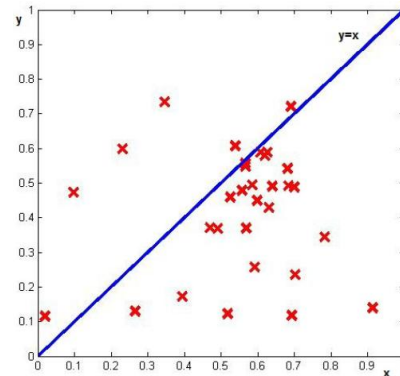


Figure13. H1 Equality test between the reference projection and mammography

According to these results a conclusion could be drawn which consists of the fact that the reduction of the x-ray dose has an effect on the estimation of the different indices of  $H$ .

### IV. DISCUSSION AND CONCLUSION

In this paper, we present two algorithms for the extraction of region of interest. We also describe statistical tests on the ROI databases gathered to see whether the model of Fractional Brownian Field helps apprehend the anisotropy of the breast. We end up with the following results:

When it comes to 3D images, tests done on tomosynthesis reveal that, at a significance level of 5%, and with a sub-sampling factor  $v$  of 3, our estimator is more likely to be biased and therefore unable to detect anisotropy.

When we increase this subsampling factor to 4, we note that the estimator improves and therefore is able to detect anisotropy.

When comparing indices computed on both mammograms and the reference tomosynthesis projection which differ on the amount of the x-ray the patient receives, we note that indices computed on mammograms are not equals to those computed

on tomosynthesis projections, this suggests that the reduction of xray dose has an effect on the estimation of H and therefore on the analysis of anisotropy.

#### REFERENCES

- [1] A.Tingberg. X-ray tomosynthesis: a review of its use for breast and chest imaging. Radiation protection dosimetry, March 2010.
- [2] Pierre Bleuet. Reconstruction 3D par tomosynthese generalisee. Application a l'imagerie medicale par rayons X. PhD thesis, ENSPG Grenoble, 2002.
- [3] Aline Bonami and Anne Estrade. Anisotropic analysis of some gaussian models. Journal of Fourier Analysis and Applications, 9(3), 2003.
- [4] Olivier Le Cadet. Classification de textures pour la caracterisation de tumeurs cerebrales. Technical report, Laboratoire de Modelisation et Calcul de l'IMAG.
- [5] C.Umarani, L.Ganesan, and S. Radhakrishnan. Combined statistical and structural approach for unsupervised texture classification. International Journal of Imaging Science and Engineering (IJISE), 2(1), JANUARY 2008.
- [6] James T. Dobbins and H.McAdams. Chest tomosynthesis: Technical principles and clinical update. European Journal of Radiology, 2009.
- [7] James T Dobbins and Devon J.Godfrey. Digital x-ray tomosynthesis: current state of the art and clinical potential. Journal of Physics in Medicine and Biology48(3):65-106,September2003.
- [8] FDA: Food and Drug Administration. <http://www.fda.gov/radiationemittingproducts/radiationemittingproductsandprocedures/medicalimaging/medicalx-rays/ucm175028.htm>, March 2011.
- [9] Rachid JENNANE, Rachid HARBA, and Gerard JACQUET. Analysis methods for fractional brownian motion: theory and comparative results. Traitement du Signal, 18(5), 2001.
- [10] Rachid JENNANE, Rachid HARBA, Emmanuel PERRIN, Aline BONAMI, and Anne ESTRADE. Analyse de champs browniens fractionnaires anisotropes, 18eme colloque du gretsi. 2001.
- [11] Mohammed Jirari. Computer Aided System For Detecting Masses in Mammograms. PhD thesis, Kent State University, 2008.
- [12] Benoit Mandelbrot and John W.Van Ness. Fractional brownian motions, fractional noises and applications. SIAM Review, 10(4):422-437, October 1968.
- [13] RSNA: Radiological Society of North America and ACR: American College of America. <http://www.radiologyinfo.org/en/info.cfm?pg=mammo>, March 2010.
- [14] Frederic Richard and Hermine Bierme. A statistical methodology for testing the anisotropy of brownian textures with an application to full-field digital mammography. October 2007.
- [15] Frederic Richard and Hermine Bierme. Estimation of anisotropic gaussian fields through radon transform. Journal of Mathematical Imaging and Vision, 12:30-50, January 2008.
- [16] Frederic Richard and Hermine Bierme. Statistical tests of anisotropy for fractional brownian textures. application to full field digital mammography. Journal of Mathematical Imaging and Vision, 36(3):227-240, March 2010.
- [17] Frederic Richard and Hermine Bierme. Analysis of texture anisotropy based on some gaussian fields with spectral density. analysis of texture anisotropy through extended fractional brownian fields. February 2011.
- [18] Andrew Smith. <http://www.promedica.org/resources/pci/services/breast-tomosynthesis.pdf>.
- [19] San Diego State University. <http://www.sci.sdsu.edu/classes/biology/bio595/paolini/computed%20tomography%20fall%2003%20v1.pdf>.
- [20] virtual medical centre. <http://www.virtualmedicalcentre.com/diseases.asp>, April 2010.